Anion-Directed Assembly of a Bimetallic Pd/Ag Nanocluster: Synthesis, Characterization, and HER Activity

Yu-Rong Ni , Rugma T P , Michael Nivendran Pillay , Tzu-Hao Chiu , Samia Kahlal , Jean-Yves Saillard * , Chen-Wei Liu *

Posted Date: 24 December 2024

doi: 10.20944/preprints202412.2078.v1

Keywords: Palladium; nanocluster; silver; hydride; hydrogen evolution

Article

Anion-Directed Assembly of a Bimetallic Pd/Ag Nanocluster: Synthesis, Characterization, and HER Activity

Yu-Rong Ni [1], Rugma T. P. [1], Michael N. Pillay [1], Tzu- Hao Chiu [1], Samia Kahlal [2], Jean-Yves Saillard [2,*] and C. W. Liu [1,*]

[1] Department of Chemistry, National Dong Hwa University, Hualien 97401, Taiwan (Republic of China).

[2] Univ Rennes, CNRS, ISCR-UMR 6226, F-35000 Rennes, France.

* Correspondence: jean-yves@univ-rennes1.fr (J.-Y.S.); chenwei@gms.ndhu.edu.tw (C.W.L.)

Abstract: Palladium-doped silver nanoclusters (NCs) have been highlighted for their unique physicochemical properties and potential applications in catalysis, optics, and electronics. Anion-directed synthesis offers a powerful route to control the morphology and properties of these NCs. Herein, we report a novel Pd-doped Ag NC, $[Pd(H)Ag_{13}(S)\{S_2P(O^iPr)_2\}_{10}]$ (**$PdHAg_{13}S$**), synthesized through the inclusion of sulfide and hydride anions. This NC features a unique linear S-Pd-H axis enclosed in a 4-5-4 stacked arrangement of silver atoms. The distinctive hydride environment was characterized by NMR spectroscopy, and the total structure was determined by single-crystal X-ray diffraction (SCXRD) and supported by computational studies. Mass spectrometry and X-ray photoelectron spectroscopy (XPS) further confirmed the assigned composition. This unique construct exhibits promising hydrogen evolution reaction (HER) activity. Our findings highlight the potential of anion-directed synthesis for creating novel bimetallic NCs with tailored structures and catalytic properties.

Keywords: Palladium; nanocluster; silver; hydride; hydrogen evolution

1. Introduction

The pursuit of atomically precise nanomaterials has led to the rapid expansion of nanocluster (NC) research [1–3]. These ultrasmall metal clusters, typically composed of a few to hundreds of atoms, bridge the gap between individual atoms and bulk materials. Unlike their bulk counterparts, NCs exhibit unique size-dependent properties from quantum confinement effects and the high proportion of surface atoms [4]. Among bimetallic systems, the combination of palladium and silver has long been exploited for their resistance to tarnish, a common problem with traditional sterling silver. On the nanoscale, the combination of metals can lead to synergistic effects, where the resulting properties are not merely a sum of the individual components but expanded functionalities compared to their monometallic counterparts. The controlled synthesis of Pd-doped Ag NCs with well-defined structures remains a significant challenge. Achieving precise control over the size, composition, and atomic arrangement is crucial for tailoring their properties and optimizing their performance.

Anion-directed synthesis has emerged as a powerful tool for manipulating the structure and composition of NCs. Anions are not limited to capping agents but can actively direct the arrangement of metal atoms as templates, influencing the overall morphology of the NC [5–8]. Halides have provided this service, and a recent publication highlights their crucial role in forming vertex-sharing Pd and Pt-doped clusters [9–12]. The selective use of sulfides in assembling atomically precise nanoclusters was first exploited by Fenske and co-workers, who reported a series of large metallic frameworks and exploited the cooperative stabilization of chalcogens and ligands in large silver

 doi:10.20944/preprints202412.2078.v1

assemblies very early on [13–15]. Various NC morphologies have been identified due to the versatility of the sulfide [13,14], including the recently reported [$PdAg_{16}(S)_2\{S_2P(OR)_2\}_{12}$] [16–18]. However, rare is the combination of two different anions, and this report highlights the combination of sulfide and hydride. Considering the ability of hydrides to occupy interstitial sites within Pd/Ag metallic frameworks, we pursued the isolation of NC containing both hydride and sulfide [19,20].

We report a novel molecule [$Pd(H)Ag_{13}(S)\{S_2P(O^iPr)_2\}_{10}$] (**$PdHAg_{13}S$**), featuring a distinct linear S-Pd-H axis encapsulated by a silver cage and dithiophosphate (dtp) passivating layer. A suite of characterization techniques, including NMR spectroscopy, single-crystal X-ray diffraction (SCXRD), and computational studies, are applied to elucidate the NC's composition, structure, and bonding. Furthermore, we explore the catalytic activity of this novel construct for the hydrogen evolution reaction (HER), a key process in sustainable energy production.

2. Results and Discussion

The cleavage of the P-S bond from the dtp ligand and the generation of the sulfide anions were indicated by our previous report [17,18]. Tuning the stoichiometric ratios of the starting materials and reducing reagent $LiBH_4$, we are able to isolate a novel NC with two hetero anions of the type [$Pd(H)Ag_{13}(S)\{S_2P(O^iPr)_2\}_{10}$] (**$PdHAg_{13}S$**), with known by-products [$Ag_7(H)\{S_2P(O^iPr)_2\}_{12}$] and [$PdAg_{20}\{S_2P(O^iPr)_2\}_{12}$], Scheme 1 [19,20].

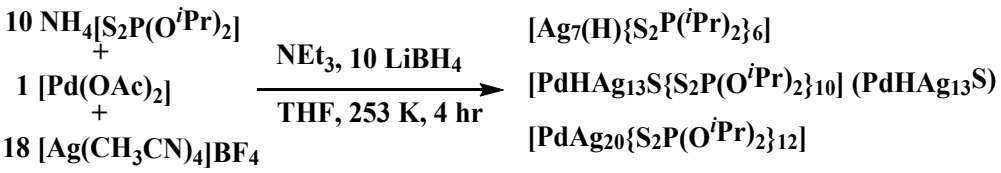

Scheme 1. Synthetic methodology for incorporation of sulfide and hydride.

The purity and composition of the isolated NC was confirmed by mass spectroscopy. The ESI-TOF-MS spectrum indicates the formation of both silver and sodium adducts during ionization with peaks obtained at *m/z* 3782.1853 Da assigned to [**$PdHAg_{13}S$**+Ag]$^+$ (Calc: *m/z* 3782.3404 Da) and *m/z* 3697.9587 Da for [**$PdHAg_{13}S$**+Na]$^+$ (Calc: *m/z* 3697.4614Da), Figure 1. The cluster is prone to decomposition during the ionization process, with the peaks assigned to several smaller silver clusters, Figure S1. The XPS analysis further establishes the cluster's compositions and verifies that Pd(0) and the Ag approaching Ag(I) are based on their distinctive binding energies (Figure S2).

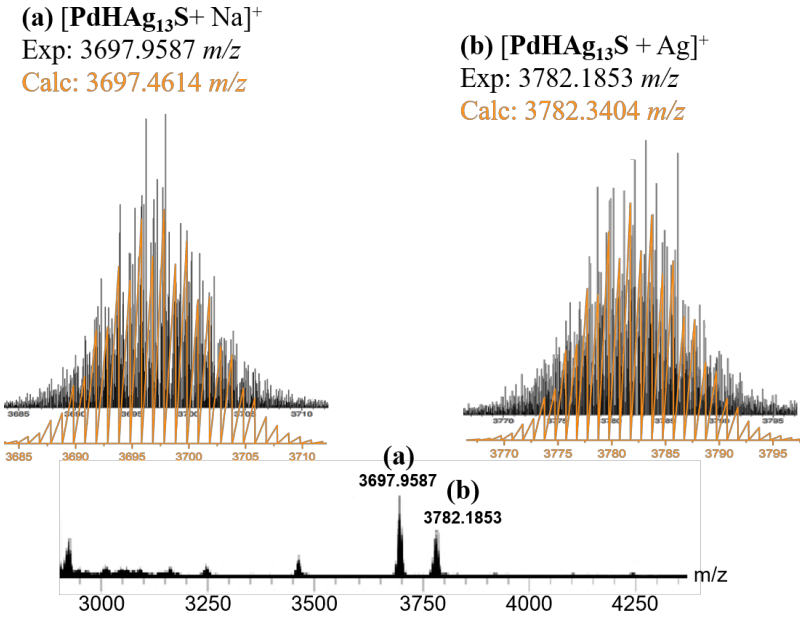

 doi:10.20944/preprints202412.2078.v1

Figure 1. The ESI-TOF-MS spectrum of **PdHAg$_{13}$S**. The positive-ion peaks with both silver and sodium adducts peaks for (a) and (b) in black, with simulated isotopic distribution overlayed in orange.

This bimetallic nanocluster exhibits a unique palladium-centered Ag_9 kernel, and $Pd@Ag_9$ metallic framework (Figure 2a). The central Ag_5 motif is sandwiched between Pd and S atoms and capped by two Ag_4 motifs (Figure 2b). Notably, the μ_5 hydride resides within a square pyramidal cavity formed by Pd and four Ag atoms (Figure 2c). This arrangement, where a hydrogen atom occupies an interstitial site within a metal framework, is characteristic of interstitial hydride systems [2]. The axis connecting the S, Pd, and H atoms (S-Pd-H) is almost perpendicular to the plane of the Ag_5 motif, deviating by 5.92°. This moderate tilt contributes to the C_1 symmetry observed in the solid state. The Pd-S bond, measuring 2.26 Å, is notably shorter than in traditional molecular complexes. The passivating layer contains three η_3 (μ_2, μ_1) and eight η_4 (μ_2, μ_2) ligands, resulting in an overall neutral configuration [1].

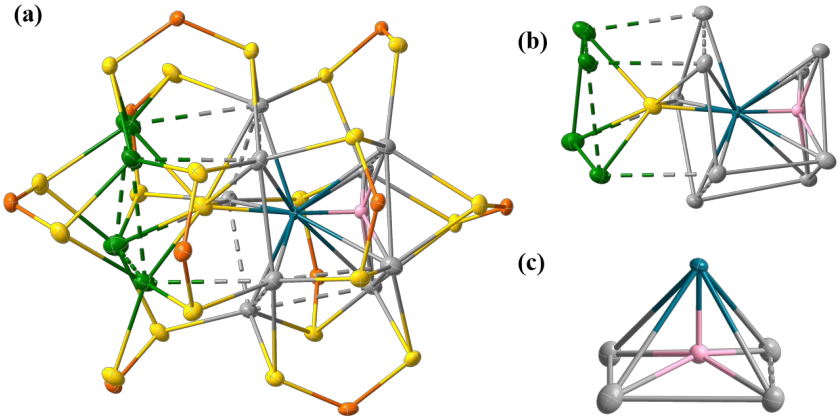

Figure 2. (a) Molecular representation of **PdHAg$_{13}$S** (ligand carbon and hydrogen atoms omitted for clarity) ellipsoid drawn at 35%, Metallic framework (b), and interstitial hydride (c). (Color code: Pd, blue; Ag_{ker}, gray; Ag_{out}, green; S, yellow; P, orange).

The $^{31}P\{^1H\}$ NMR spectrum displays a single resonance at 102.32 ppm at ambient temperature (Figure S3a), indicating a time-averaged equivalence of all phosphorus atoms resulting from the dynamic processes. However, upon cooling to 213 K, the peak splits into five distinct resonances, correlating to non-equivalent phosphorus environments observed in the solid state (Figure S4a). The disorder observed in the solid state is also present in the solution, as evidenced by ^1H NMR data. A multiplet resonance was observed at -3.98 ppm (Figure S3b), confirming the presence of a hydride. Notably, the integration ratio of the ^1H NMR spectrum further supports the assignment of ten dtp ligands per single hydride and correlates to isopropyl substituents. The multiplicity observed indicates that the hydride couples to several Ag nuclei due to the dynamic nature of the hydride. This observation is consistent with the dynamic *flipping* of the S-Pd-H axis observed in the solid-state structure. Furthermore, the variable temperature NMR (VT-NMR) experiments indicate that the hydride resonance remains broad at low temperatures (213 K), suggesting residual mobility (Figure S4b). In solution, the dynamic behavior of this encapsulated unit, coupled with the fluxionality of the ligand shell, is expected to play a crucial role in the cluster's effectiveness as an electrocatalyst for hydrogen evolution reactions (HER).

A key goal in tailoring NC is the tuning of optical properties, and incorporating sulfide yields an emissive NC. Comparing previously reported silver-rich palladium NC, **PdHAg$_{13}$S** has the shortest emissive wavelength reported for chalcogen-passivated NCs [19–22]. The optical spectrum for **PdHAg$_{13}$S**, with an absorption maximum centered at 356 nm (Figure 3), is similar to the previously reported $[PdAg_{16}S_2\{S_2P(O^iPr)_2\}_{12}]$, 365 nm [18]. However the emission wavelength is blue shifted (λem = 681 nm, τ = 121.1 μs) (Figure S5) compared to $[PdAg_{16}S_2\{S_2P(O^iPr)_2\}_{12}]$ (λem = 808 nm, τ = 92.3 μs).

Preprints.org (www.preprints.org) | NOT PEER-REVIEWED | Posted: 24 December 2024 doi:10.20944/preprints202412.2078.v1

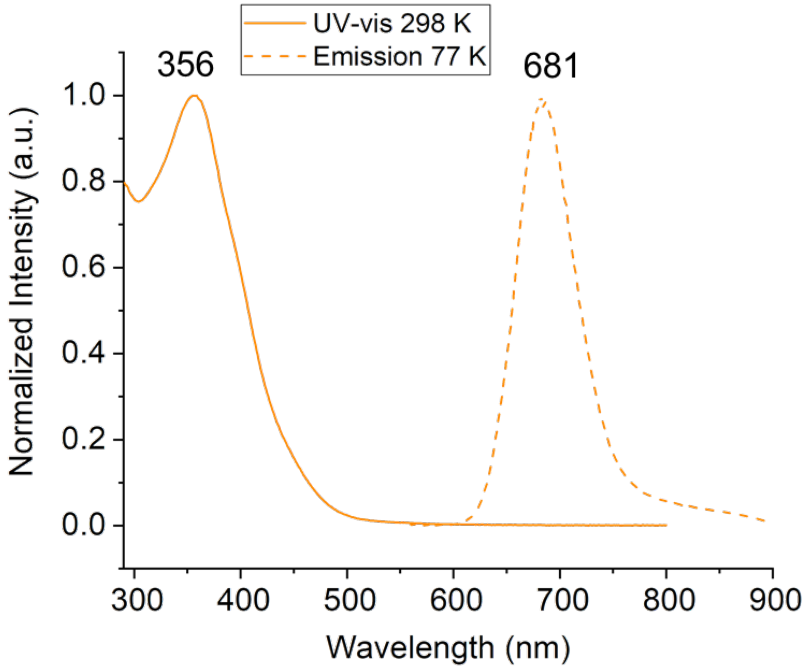

Figure 3. Optical spectra for **PdHAg$_{13}$S** recorded in 2-MeTHF.

The DFT-optimized geometry was performed on a simplified model for **PdHAg$_{13}$S**, [Pd(H)Ag$_{13}$(S)(S$_2$PH$_2$)$_{10}$] to gain insights into its structure and electronic properties. The optimized geometry obtained from these calculations is in good agreement with the structure determined by single-crystal X-ray diffraction (SCXRD) (see Table 1 and the corresponding XYZ file in Table S1).

Table 1. Comparison of structural observations experimental and computed.

NC	SXRD	DFT
Pd-S	2.259(7)	2.315
Pd-Ag$_{ker}$	2.778(9)-3.021(7) avg. 2.872(8)	2.848-3.086 avg. 2.956
Ag$_{ker}$-Ag$_{ker}$	2.893(6)-3.114(6) avg. 2.989(6)	2.988-3.155 avg. 3.051
Ag$_{out}$-Ag$_{out}$	3.043(7)-3.156(7) avg. 3.090(7)	3.120-3.190 avg. 3.155
Ag$_{ker}$-S	2.665(12)-2.915(12) avg. 2.777(12)	2.779-2.845 avg. 2.812
Ag$_{out}$-S	2.568(12)-2.903(9) avg. 2.745(9)	2.786-2.975 avg. 2.881

Analysis of the computed data supports the view of describing the whole NC as made of a quasi-linear [SPdH]$^{3-}$ 14-electron complex stabilized by a shell of 13 Ag(I) centers, Table 2 and Figure S6. Two significantly different Ag(I) environments can be distinguished as nine Ag(I) atoms coordinated to the Pd(0) atom (Ag$_{ker}$) and four outer Ag(I) atoms (Ag$_{out}$) anchored by a μ_7 sulfide. NAO atomic charges (Table 2) support this assignment. Four Ag$_{ker}$ atoms form a square pyramid, with the Pd atom encapsulating an interstitial μ_5 hydride. The Pd-H and Pd-S bonds exhibit significant covalent character, as evidenced by their relatively large Wiberg bond indices (WBIs, Table 2). The Ag-S(dtp) bonds also show substantial covalent character. In addition to these covalent interactions, metallophilic interactions between the silver atoms contribute to the stability of the NC, as exemplified by the Ag…Ag WBI values which are typical for such type of interaction (Table 2). The Kohn-Sham orbital diagram (Figure S6) provides further insights into the electronic structure. The highest occupied molecular orbitals (HOMOs) are primarily composed of 4d(Pd) and 3p(S), whereas the lowest unoccupied molecular orbitals (LUMOs) are 5p(Pd) and 5s/5p(Ag$_{ker}$). Time-dependent

 doi:10.20944/preprints202412.2078.v1

DFT (TD-DFT) calculations were performed to simulate the UV-vis spectrum. The calculated UV-vis spectrum is in reasonable agreement with the experimental spectrum, Figure S7. It shows a low-energy band attributed to the HOMO-1 → LUMO+2, HOMO-1 → LUMO+1 and HOMO-2 → LUMO transitions, thus of 4d(Pd)/3p(S) → 5s/5p(Ag_{ker}) nature. These transitions involve charge transfer from the Pd and S atoms to the Ag atoms.

Table 2. Natural atomic orbital (NAO)-computed atomic charges and Wiberg bond indices (WBI).

Atom	NAO charge	Bond	WBI
Pd	-0.58	Pd-H	0.373
H	-0.42	Pd-S	0.303
S	-1.28	Ag-H	0.057
Ag_{ker}(avg)	0.68	Pd-Ag_{ker}(avg)	0.069
Ag_{out}(avg)	0.72	Ag_{ker}-S(avg)	0.087
		Ag_{out}-S(avg)	0.057
		Ag-Ag(avg)	0.039
		Ag-S(dtp) (avg)	0.141

Hydrogen is widely regarded as a highly promising energy source because of its environmental sustainability and zero-emission properties. The electrocatalytic HER plays a crucial role in renewable and clean energy initiatives. Noble metals like Pt and Pd are known for their exceptional electrocatalytic efficiency in HER, largely due to their optimal hydrogen binding energy, favorable Gibbs free energy for atomic hydrogen adsorption, and low activation barriers for hydrogen desorption. Although silver is typically considered one of the least reactive metals in HER processes, the cost-effectiveness and abundance of silver-based nanomaterials have sparked interest in investigating their potential for hydrogen evolution [23–25]. The HER activity of **$PdHAg_{13}S$** was compared with related sulfide containing [$Pd_6Ag_{14}(S)\{S_2P(OPr)_2\}_{12}$] (**$Pd_6Ag_{14}S$**) [21], and [$PdAg_{16}(S)_2\{S_2P(O^iPr)_2\}_{12}$] (**$PdAg_{16}S_2$**) [18], by linear sweep voltammetry (LSV) in a three-electrode electrochemical cell containing an argon saturated 0.5 M H_2SO_4 solution, (Figure 4a). **$Pd_6Ag_{14}S$** and **$PdHAg_{13}S$** exhibit a higher HER activity than **$PdAg_{16}S_2$**. The overpotentials to reach a current density of -10 $mAcm^{-2}$ were found to be -290, -345, and -542 mV for **$Pd_6Ag_{14}S$**, **$PdHAg_{13}S$**, and **$PdAg_{16}S_2$**, respectively, indicating that **$Pd_6Ag_{14}S$** is the most efficient H_2-producing electrocatalyst in the series. The Tafel slope is used to evaluate the kinetics of the HER, **$Pd_6Ag_{14}S$**, **$PdHAg_{13}S$**, and **$PdAg_{16}S_2$**, **which** are 129, 137, and 182 mV/dec, respectively (Figure 4b). A lower Tafel slope typically indicates more efficient electron transfer, leading to faster reaction rates. **$Pd_6Ag_{14}S$**, and **$PdHAg_{13}S$** clusters, with Tafel slopes of 129 and 137 mV/dec, have relatively more efficient HER kinetics compared to **$PdAg_{16}S_2$** (182 mV/dec). Furthermore, the Tafel slopes of **$Pd_6Ag_{14}S$ and $PdHAg_{13}S$** are closer to the theoretical Tafel slope of the Volmer step (120 mV/dec), indicating proton adsorption is the rate-determining step. The improved efficiency of the silver sites compared to monometallic clusters [26] is due to the synergistic effect of the Pd atom encapsulated by the silver metallic framework. For instance, $Pd_6Ag_{14}S$ exhibits a slightly lower overpotential and Tafel slope for HER compared to $PdHAg_{13}S$, likely due to the higher number of Pd atoms present in the cluster. However, in comparison to open Pd sites, such as those found in [$PdHCu_{11}\{S_2P(O^iPr)_2\}_6(C{\equiv}CPh)_4$] [27], the performance is significantly lower. Further highlighting that the defect engineering or ligand modifications may help reveal the reactions on Pd of these clusters, which potentially enhance their activity for HER.

 doi:10.20944/preprints202412.2078.v1

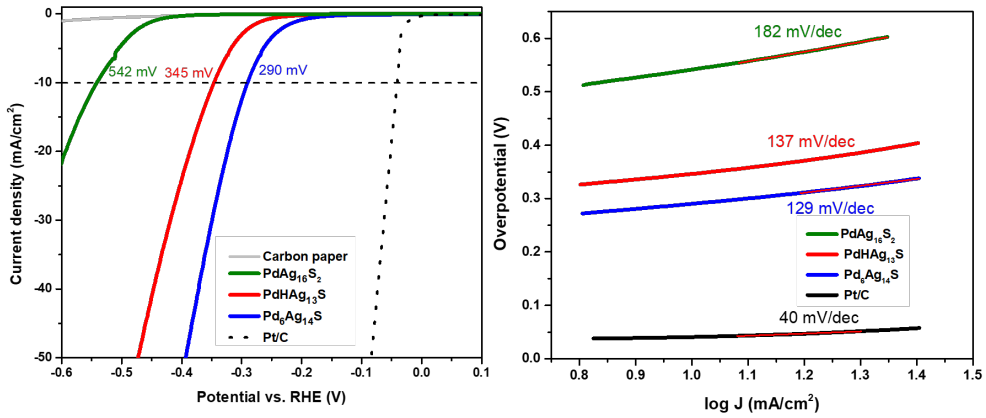

Figure 4. (a) LSVs recorded at 1 mV s^{-1} for **$Pd_6Ag_{14}S$**, **$PdHAg_{13}S$**, **$PdAg_{16}S_2$**, Pt/C, and carbon paper; (b) Tafel slopes of **$Pd_6Ag_{14}S$**, **$PdHAg_{13}S$**, **$PdAg_{16}S_2$**, and Pt/C.

3. Materials and Methods

All reactions were conducted using standard Schlenk protocols under an inert N_2 environment. All chemicals were used as supplied from commercial sources, including palladium(II) acetate ($PdOAc_2$, 98%) and lithium borohydride ($LiBH_4$, 2 M in THF). $[Ag(MeCN)_4]BF_4$ [28] and $NH_4[S_2P(O^iPr)_2]$ [29] were prepared according to previous reports. NMR and VT-NMR spectra were recorded on a Bruker Advance II 400 spectrometer, operating at 400 MHz for ^1H and 161.97 MHz for $^{31}P\{^1H\}$. ESI-TOF-MS spectra were recorded on a Fison Quattro Bio-Q (Fisons Instruments, VG Biotech, UK). The XPS spectra were recorded using a PHI 5000 VersaProbe-Scanning ESCA Microprobe on an X-ray Photoelectron Spectrometer. The absorption spectrum was recorded on an Agilent Cary-60 spectrometer. The PL spectra and lifetime decays were measured in an EPR tube with a liquid cryogenic system at 77 K and were recorded on a HORIBA FluoroMax plus spectrometer.

SCXRD Analysis

Paratone oil was used to coat and mount a single crystal onto a glass fiber. Data were recorded with a graphite mono-chromated Mo-Kα radiation source (λ=0.71073 Å) fitted on a Bruker APEX II CCD diffractometer operating at 100 K. Data analysis was done with SADABS and SAINT, for adsorption corrections on raw data frames [30,31]. SHELXL-2018/3 package integrated into SHELXL/PC V6.14. [32–34] was used to solve the structure and then refined using least-squares versus F^2. Anisotropic refinements were applied to all non-hydrogen atoms. Structure refinement details are summarized below in Table 3.

Table 3. Crystal data and refinement of **$PdHAg_{13}S$**.

Compound	**$[PdHAg_{13}S\{S_2P(O^iPr)_2\}_{10}]$**
Chemical formula	$C_{60}H_{141}Ag_{13}O_{20}P_{10}PdS_{21}$
CCDC	2411564
Formula weight	3674.39
Crystal system, space group	Monoclinic, C2/c
a, Å α, deg	54.746(3) 90
b, Å β, deg	17.9162(9) 99.799(2)
c, Å γ, deg	27.3550(14) 90
Volume, $Å^3$	26439
Z	8
ϱcalcd, $g{\cdot}cm^{-3}$	1.846
μ, mm^{-1}	2.510

 doi:10.20944/preprints202412.2078.v1

Temperature, K	100(2)
θmax, deg. / Completeness, %	25.000 / 100
Reflections collected / unique	140003 / 23299
Restraints/parameters	364 / 1176
R1a, wR2b [I > 2σ(I)]	0.0381, 0.0751
R1a, wR2b (all data)	0.0510, 0.0804
Goodness of fit	1.051
Largest diff. peak and hole, e/Å^3	2.418 and -1.748

[a]$R1 = \Sigma | |F_o| - |F_c| | / \Sigma |F_o|$. [b]$wR2 = \{ \Sigma [w(F_o^2 - F_c^2)^2] / \Sigma [w(F_o^2)_2] \}^{1/2.}$

Computational Methods

The geometry optimization was performed by density functional theory (DFT) calculations with the Gaussian16 package, [35] with a BP86 functional [36,37] and the all-electron Def2-TZVP basis set from the EMSL Basis Set Exchange Library [38,39]. The optimized geometries were characterized as true minima through vibrational analysis. The natural atomic orbital (NAO) charges and the Wiberg bond indices (WBI) were computed with the NBO6.0 program [40,41] on single-point calculations performed with the BP86 functional and the Def2-SVP basis set for computational limitations [42,43]. The UV-visible transitions were calculated by means of time-dependent DFT (TD-DFT) calculations, with the CAM-B3LYP functional [44] and the Def2-TZVP basis set. The UV-visible spectra were simulated from the computed TD-DFT transitions and their oscillator strengths by using the Multiwfn program [45]. The compositions of the molecular orbitals were calculated using the AOMix program [46].

Electrocatalytic Measurements

Electrode preparation: The catalyst ink was prepared by sonicating the mixture of the nanocluster and CH_2Cl_2 for 20 min. 3 nmol of the catalyst ink was loaded onto a carbon paper (1 cm^2), which was air-dried overnight before use.

Electrochemical measurements: Measurements were performed on an Admiral Instruments: Squidstat Plus Potentiostat. A three-electrode electrochemical cell consisting of a catalyst-immobilized carbon paper electrode, a Pt foil anode (3 cm^2), and an Ag/AgCl reference electrode. The electrolyte solution of 0.5 M H_2SO_4 was degassed with Ar gas for 30 min before the electrochemical measurements. For comparison, a benchmark Pt/C electrode was prepared by drop casting 200 µL of a catalyst ink, made by dispersing 10 mg of Pt/C with 200 µL of 5 wt% Nafion solution, in 800 µL of isopropyl alcohol, onto carbon paper. Electrode potential measured was converted to the RHE scale using the following equation: $E_{RHE} = E_{Ag/AgCl} + 0.197 + 0.059\ pH$ (1)

Synthesis of [Pd(H)Ag$_{13}$(S){S$_2$P(O^{i}Pr)$_2$}$_{10}$], PdHAg$_{13}$S

[NH_4] [$S_2P(O^iPr)_2$] (0.26 g, 1.13 mmol), [$Pd(OAc)_2$] (0.025 g, 0.11 mmol), [$Ag(CH_3CN)_4$]BF_4 (0.74 g, 2.06 mmol), NEt_3 (100 µl, 0.717 mmol) and THF (20 mL) were added in the reaction flask for 20 min. $LiBH_4$ (0.3 mL, 0.59 mmol) was added with vigorous stirring at 253 K. The color of the solution gradually changed from orange to brown. After 4 hours, the mixture was evaporated, and the residue was extracted with DCM and washed water. Column chromatography with Al_2O_3 was used to purify the yellow targeted product with mixed solvent DCM and ether (v:v=5:1), [Pd(H)Ag$_{13}$(S){S$_2$P(O^{i}Pr)$_2$}$_{10}$], 0.86 % yield. The byproducts further used the solvent ratio (10:1) and (1:1) to yield [Ag$_7$(H){S$_2$P(O^{i}Pr)$_2$}$_6$] in 18.6% and [PdAg$_{20}${S$_2$P(O^{i}Pr)$_2$}$_{12}$] in 31.6%, based on Pd. ^{1}H NMR (400 MHz, $(CD_3)_2CO$, δ, ppm, 298 K): 4.94 (septet, CH, 20H), 1.39 (d, CH_3, 120H); -3.98($^1J_{HAg}$ = 13.2 Hz). VT ^{1}H NMR (400 MHz, $(CD_3)_2CO$, δ, ppm, 213 K): -3.66. ^{31}P{^{1}H} NMR (161.97 MHz, $(CD_3)_2CO$, δ, ppm, 298 K): 102.32. VT ^{31}P{^{1}H} NMR (161.97 MHz, $(CD_3)_2CO$, δ, ppm, 213 K): 104.21, 102.57, 102.46, 102.25, 101.69. ESI-MS (*m*/*z*): exp. 3782.1853 (calc.3782.3404 for [PdHAg$_{13}$S +Ag]$^+$) and exp. 3697.9587 (calc. 3697.4614 for [PdHAg$_{13}$S +Na]$^+$). UV-Vis [λ_{max} in nm, (ε in M^{-1}cm^{-1})]: 356 (66023). XPS (Calc.: Pd%0.95,

 doi:10.20944/preprints202412.2078.v1

Ag%12.38, S%20.00, P%9.52, C%57.14): Pd%0.94, Ag%12.40, S%20.07, P%9.50, C%57.09, and (binding energy, eV): Ag $3d_{5/2}$, 367.55; Ag $3d_{3/2}$, 373.55; Pd $3d_{5/2}$, 337.31; Pd $3d_{3/2}$, 342.57.

4. Conclusions

This study successfully demonstrated the anion-directed synthesis of a novel palladium-doped silver nanocluster featuring a unique linear S-Pd-H unit which can be described as a $[SPH]^{3-}$ anionic complex encapsulated within. Incorporating sulfide and hydride anions was crucial in directing the morphology. Comprehensive characterization, including NMR spectroscopy, single-crystal X-ray diffraction (SCXRD), and computational studies, provided detailed insights into the NC's composition, structure, and electronic properties. The NC exhibits promising catalytic activity for the hydrogen evolution reaction (HER), underscoring the potential of anion-directed synthesis as a powerful strategy for creating bimetallic NCs with tailored structures and properties for catalytic applications. Future research will explore the detailed mechanism of HER cata by this NC and investigate the effects of ligand modification and alloying with other metals on its catalytic performance. Ultimately, this work opens new avenues for the design and synthesis of bimetallic nanoclusters with enhanced properties.

Supplementary Materials: The following supporting information can be downloaded at the website of this paper posted on Preprints.org.

Author Contributions: Y.-R. N., R. T. P., T.-H. C., M. N. P., Investigation, data curation, Formal analysis, methodology, writing. S. K. data curation, formal analysis. J.-Y. S. data curation, formal analysis, writing. C. W. L. supervision, writing, conceptualization, project administration, resources.

Funding: This work was supported by the National Science and Technology Council of Taiwan (113-2123-M-259-001).

Data Availability Statement: Crystallographic data for [**1**] has been deposited at the Cambridge Crystallographic Data Centre under [CCDC 2411564] and can be obtained from www.ccdc.cam.ac.uk/data_request/cif. Computational details (including coordinate file), X-ray structure analyses, NMR spectra, electrochemical data, ESI-MS data, and luminescence decay curves are available in the Supplementary Information.

Acknowledgments: This work was supported by the National Science and Technology Council of Taiwan (113-2123-M-259-001) and the GENCI French National Computer Resource Center (A0030807367).

Conflicts of Interest: "The authors declare no conflicts of interest."

References

1. Artem'ev, A. V; Liu, C.W. Recent Progress in Dichalcophosphate Coinage Metal Clusters and Superatoms. *Chem. Commun.*, **2023**, *59*, 7182–7195.
2. Chiu, T.-H.; Liao, J.-H.; Silalahi, R.P.B.; Pillay, M.N.; Liu, C.W. Hydride-Doped Coinage Metal Superatoms and Their Catalytic Applications. *Nanoscale Horiz.* **2024**, *9*, 675–692.
3. Yang, J.; Jin, Rongchao. New Advances in Atomically Precise Silver Nanoclusters. *ACS Mater. Lett.* **2019**, *1*, 482–489.
4. Wu, Z.; Yao, Q.; Zang, S.; Xie, Jianping. Directed Self-Assembly of Ultrasmall Metal Nanoclusters. *ACS Mater. Lett.* **2019**, *1*, 237–248.
5. Liao, J.-H.; Chen, H.; You, H.-J.; Liu, C.W. Oxocarbon Anions Templated in Silver Clusters. *Inorg. Chem.* **2022**, *61*, 14115–14120.
6. Chang, H.-W.W.; Liao, J.H.-H.; Li, B.; Chen, Y.J.-J.; Liu, C.W. Trigonal Pyramidal Oxyanions as Structure-Directing Templates for the Synthesis of Silver Dithiolate Clusters. *J. Struct. Chem.* **2014**, *55*, 1426–1432.
7. Liao, J.-H.; Chang, H.-W.; You, H.-C.; Fang, C.-S.; Liu, C.W. Tetrahedral-Shaped Anions as a Template in the Synthesis of High-Nuclearity Silver(I) Dithiophosphate Clusters. *Inorg. Chem.* **2011**, *50*, 2070–2072.

8. Sun, D.; Wang, H.; Lu, H.-F.; Feng, S.-Y.; Zhang, Z.-W.; Sun, G.-X.; Sun, D.-F. Two Birds with One Stone: Anion Templated Ball-Shaped Ag56 and Disc-like Ag20 Clusters. *Dalton Trans.* **2013**, *42*, 6281-6284.
9. Miyajima, S.; Hossain, S.; Ikeda, A.; Kosaka, T.; Kawawaki, T.; Niihori, Y.; Iwasa, T.; Taketsugu, T.; Negishi, Y. Key Factors for Connecting Silver-Based Icosahedral Superatoms by Vertex Sharing. *Commun. Chem.* **2023**, *6*, 57.
10. Zhong, Y.J.; Liao, J.H.; Chiu, T.H.; Wen, Y.S.; Liu, C.W. A New Synthetic Methodology in the Preparation of Bimetallic Chalcogenide Clusters via Cluster-to-Cluster Transformations. *Molecules* **2021**, *26*, 5391.
11. Liu, C.W.; Haia, H.C.; Hung, C.M.; Santra, B.K.; Liaw, B.J.; Lin, Z.; Wang, J.C. New Halide-Centered Discrete Ag^{I}_{8} Cubic Clusters Containing Diselenophosphate Ligands, $\{Ag_8(X)\ [Se_2P(OR)_2]_6\}(PF_6)$ (X = Cl, Br; R = Et, Pr, ^{i}Pr): Syntheses, Structures, and DFT Calculations. *Inorg. Chem.* **2004**, *43*, 4464–4470.
12. Liu, C.W.; Hung, C.M.; Chen, H.C.; Wang, J.C.; Keng, T.C.; Guo, K. A Novel Nonacoordinate Bridging Selenido Ligand in a Tricapped Trigonal-Prismatic Geometry. X-Ray Structure of $Cu_{11}(\circledcirc_9\text{-Se})(\circledcirc_3\text{-Br})_3[Se_2P(OPr))_2]_6$. *Chem. Commun.* **2000**, 1897–1898.
13. Fenske, D.; Anson, C.E.; Eichhöfer, A.; Fuhr, O.; Ingendoh, A.; Persau, C.; Richert, C. Syntheses and Crystal Structures of $[Ag_{123}S_{35}(S^tBu)_{50}]$ and $[Ag_{344}S_{124}(S^tBu)_{96}]$. *Angew. Chem. Int. Ed.* **2005**, *44*, 5242–5246.
14. Wang, X.-J.; Langetepe, T.; Persau, C.; Kang, B.-S.; Sheldrick, G.M.; Fenske, D. Syntheses and Crystal Structures of the New Ag–S Clusters $[Ag_{70}S_{16}(SPh)_{34}(PhCO_2)_4(Triphos)_4]$ and $[Ag_{188}S_{94}(PR_3)_{30}]$. *Angew. Chem. Int. Ed.* **2002**, *41*, 3818–3822.
15. Bestgen, S.; Yang, X.; Issac, I.; Fuhr, O.; Roesky, P.W.; Fenske, D. Adamantyl- and Furanyl-Protected Nanoscale Silver Sulfide Clusters. *Chem. Eur. J.* **2016**, *22*, 9933–9937.
16. Chang, H.W.; Shiu, R.Y.; Fang, C.S.; Liao, J.H.; Kishore, P.V.V.N.; Kahlal, S.; Saillard, J.Y.; Liu, C.W. A Sulfide (Selenide)-Centered Nonanuclear Silver Cluster: A Distorted and Flexible Tricapped Trigonal Prismatic Ag_9 Framework. *J. Clust. Sci.* **2017**, *28*, 679–694.
17. Yoshinari, N.; Goo, Z.L.; Nomura, K.; Konno, T. Silver(I) Sulfide Clusters Protected by Rhodium(III) Metalloligands with 3-Aminopropanethiolate. *Inorg. Chem.* **2023**, *62*, 9291–9294.
18. Ni, Y.-R.; Pillay, M.N.; Chiu, T.-H.; Liang, H.; Kahlal, S.; Chen, J.-Y.; Chen, Y.-J.; Saillard, J.-Y.; Liu, C.-W. Sulfide-Mediated Growth of NIR Luminescent Pd/Ag Atomically Precise Nanoclusters. *Nanoscale* **2025**, doi:10.1039/D4NR04136D.
19. Ni, Y.R.; Pillay, M.N.; Chiu, T.H.; Rajaram, J.; Wu, Y.Y.; Kahlal, S.; Saillard, J.Y.; Liu, C.W. Diselenophosphate Ligands as a Surface Engineering Tool in PdH-Doped Silver Superatomic Nanoclusters. *Inorg. Chem.* **2024**, *63*, 2766–2775.
20. Ni, Y.-R.; Pillay, M.N.; Chiu, T.-H.; Wu, Y.-Y.; Kahlal, S.; Saillard, J.-Y.; Liu, C.W. Controlled Shell and Kernel Modifications of Atomically Precise Pd/Ag Superatomic Nanoclusters. *Chem. Eur. J.* **2023**, 29, e202300730.
21. Barik, S.K.; Chiu, T.-H.; Liu, Y.-C.; Chiang, M.-H.; Gam, F.; Chantrenne, I.; Kahlal, S.; Saillard, J.-Y.; Liu, C.W. Mono- and Hexa-Palladium Doped Silver Nanoclusters Stabilized by Dithiolates. *Nanoscale* **2019**, *11*, 14581–14586.
22. Barik, S.K.; Chen, C.-Y.; Chiu, T.-H.; Ni, Y.-R.; Gam, F.; Chantrenne, I.; Kahlal, S.; Saillard, J.-Y.; Liu, C.W. Surface Modifications of Eight-Electron Palladium Silver Superatomic Alloys. *Commun. Chem.* **2022**, *5*, 151.
23. Tang, Y.; Sun, F.; Ma, X.; Qin, L.; Ma, G.; Tang, Q.; Tang, Z. Alkynyl and Halogen Co-Protected $(AuAg)_{44}$ Nanoclusters: A Comparative Study on Their Optical Absorbance, Structure, and Hydrogen Evolution Performance. *Dalton Transactions* **2022**, *51*, 7845–7850.
24. Shen, H.; Zhu, Q.; Xu, J.; Ni, K.; Wei, X.; Du, Y.; Gao, S.; Kang, X.; Zhu, M. Stepwise Construction of Ag_{29} Nanocluster-Based Hydrogen Evolution Electrocatalysts. *Nanoscale* **2023**, *15*, 14941–14948.
25. Liu, X.; Tang, Y.; Chen, L.; Wang, L.; Liu, Y.; Tang, Z. Atomically Precise $Au_{15}Ag_{23}$ Nanoclusters Co-Protected by Alkynyl and Bromine: Structure Analysis and Electrocatalytic Application toward Overall Water Splitting. *Int. J. Hydrogen Energy* **2024**, *53*, 300–307.
26. Jangid, K.D.; Dastider, S.G.; Mandal, S.; Kumar, P.; Kumari, P.; Haldar, K.; Mondal, K.; Dhayal, S.R. Ferrocenyl Dithiophosphonate Ag(I) Complexes: Synthesis, Structures, Luminescence, and Electrocatalytic Water Splitting Tuned by Nuclearity and Ligands. *Chem. Eur. J.*, *30*, e202402900.

 doi:10.20944/preprints202412.2078.v1

27. Silalahi, R.P.B.; Jo, Y.; Liao, J.; Chiu, T.; Park, E.; Choi, W.; Liang, H.; Kahlal, S.; Saillard, J.; Lee, D.; et al. Hydride-containing 2-Electron Pd/Cu Superatoms as Catalysts for Efficient Electrochemical Hydrogen Evolution. *Angew. Chem. Int. Ed.* **2023**, *62*, e202301272.
28. Aly, A.A.M.; Walfort, B.; Lang, H. Crystal Structure of Tetrakis(Acetonitrile)Silver(I) Tetrafluoroborate, $[Ag(CH_3CN)_4]$ $[BF_4]$. *Z. Kristallogr. NCS*, **2004**, *219*, 489–491.
29. Wystrach, V.; Hook, E.; Christpoher, G.L. Notes - Basic Zinc Double Salts of O,O-Diakyl Phosphorodithioic Acids. *J. Org. Chem.* **1956**, *21*, 705–707.
30. SADABS, Version 2014-11.0, Bruker Area Detector Absorption Corrections 2014.
31. SAINT, Included in G. Jogl, V4.043: Software for the CCD Detector System 1995.
32. Sheldrick, G.M. A Short History of SHELX. *Acta Cryst. A* **2008**, *64*, 112–122.
33. SHELXTL, Version 6.14 2003.
34. Gruene, T.; Hahn, H.W.; Luebben, A. V; Meilleur, F.; Sheldrick, G.M.J. Refinement of Macromolecular Structures against Neutron Diffraction Data with SHELXL2013. *J. Appl. Crystallogr.* **2014**, *47*, 462–466.
35. Frisch, M.J.; Trucks, G.W.; Schlegel, H.B.; Scuseria, G.E.; Robb, M.A.; Cheeseman, J.R.; Scalmani, G.; Barone, V.; Petersson, G.A.; Nakatsuji, H.; et al. Gaussian 16, Revision A.03 2016.
36. Becke, A.D. Density-functional Exchange-energy Approximation with Correct Asymptotic Behavior. *Phys. Rev. A* **1988**, *38*, 3098–3100.
37. Perdew, J.P. Density-Functional Approximation for the Correlation Energy of the Inhomogeneous Electron Gas. *Phys Rev B* **1986**, *33*, 8822–8824.
38. Schaefer, A.; Horn, H.; Ahlrichs, R. Fully Optimized Contracted Gaussian Basis Sets for Atoms Li to Kr. *J. Chem. Phys.* **1992**, *97*, 2571–2577.
39. Schaefer, A.; Huber, C.; Ahlrichs, R. Fully Optimized Contracted Gaussian Basis Sets of Triple Zeta Valence Quality for Atoms Li to Kr. *J. Chem. Phys.* **1994**, *100*, 5829–5835.
40. Glendening, E.D.; Landis, C.R.; Weinhold, F. Natural Bond Orbital Methods. *J. Comput. Chem.* **2013**, *34*, 1429–1437.
41. Glendening, E.D.; Badenhoop, J.K.; Reed, A.E.; Carpenter, J.E.; Bohmann, J.A.; Morales, C.M.; Landis, C.R.; Weinhold, F. NBO 6.0; Theoretical Chemistry Institute, University of Wisconsin, Madison, WI, 2013, http://nbo6.chem.wisc.edu.
42. Weigend, F. Accurate Coulomb-Fitting Basis Sets for H to Rn. *Phys. Chem. Chem. Phys.* **2006**, *8*, 1057–1065.
43. Weigend, F.; Ahlrichs, R. Balanced Basis Sets of Split Valence, Triple Zeta Valence and Quadruple Zeta Valence Quality for H to Rn: Design and Assessment of Accuracy. *Phys. Chem. Chem. Phys.* **2005**, *7*, 3297–3305.
44. Yanai, T.; Tew, D.; Handy, N. A New Hybrid Exchange–Correlation Functional Using the Coulomb-Attenuating Method (CAM-B3LYP). *Chem. Phys. Lett.* **2004**, *393*, 51–57.
45. Liu, T.; Chen, F. Multiwfn: A Multifunctional Wavefunction Analyzer. *J. Comput. Chem.* **2012**, *33*, 580–592.
46. Gorelsky, S.I.; Lever, A. B. P. Electronic structure and spectra of ruthenium diimine complexes by density functional theory and INDO/S. Comparison of the two methods. *J. Organomet. Chem*. **2001**, *635*, 187–196.